

Attitude and Orbital Dynamics Coupled Simulator For High Area-to-Mass Ratio Satellites

Cristiano Contini, Camilla Colombo

Abstract Nowadays the interest in small satellites large constellations or MicroSats in formation flying is increasing and, as a consequence, the challenges related to the Attitude Determination and Control Subsystem are increasing, being related to the capability to enhance a fine pointing budget and to be able to take into account the coupling between attitude and orbital dynamics. In this paper, an Attitude Determination and Control Subsystem simulator will be presented, fundamental to evidence the fine dynamical coupling in the ZodiArt iSEE mission, by Politecnico di Milano. The simulator is characterised by a complete disturbances model, including: the Earth zonal harmonics, the Moon and Sun third body perturbations, solar radiation pressure, drag and lift. Moreover, compact plots, here called *Orbital long-track envelope*, will be presented, graphically showing the differential gain/loss in altitude and relative long-track shift obtained performing differential drag, depending on the manoeuvre epoch, angle of attack and true anomaly.

1 Introduction

Modern spacecrafts are designed with complex shapes and large areas, in order to accomplish peculiar mission objectives, maintaining a low mass to reduce the launch cost. Moreover, the possibility to launch clusters of small satellites in formation flying is becoming reality and a precise knowledge of the relative position among the platforms will be mandatory. As a result, for Earth observation satellites, atmospheric drag and solar radiation pressure become the main actors, driv-

Cristiano Contini

Department of Aerospace Science and Technology, Politecnico di Milano, Via Giuseppe La Masa 34, Milano, 20156, ITALY, e-mail: cristiano.contini@mail.polimi.it

Camilla Colombo

Department of Aerospace Science and Technology, Politecnico di Milano, Via Giuseppe La Masa 34, Milano, 20156, ITALY, e-mail: camilla.colombo@polimi.it

ing and coupling the orbital dynamics with the attitude one. This is the case of the ZodiArt iSEE [1] project, a new mission design carried out by Politecnico di Milano and lead by Prof. Camilla Colombo, whose aim is to launch a set of MicroSat each of them equipped with a reflective balloon, to promote space advertisement during twilight time and to enhance Earth observation during day time. The challenges related to the dynamics of such a peculiar spacecraft are mostly related to the *attitude determination and control subsystem*, since the platform is characterised by high and uncommon, for this class of platforms, disturbances torques and a complex operative scenario such a constellation orbiting in formation. In the case of such complex missions the model and simulation of the spacecraft dynamics, coupled with the perturbed orbital dynamics, become of fundamental importance. In this paper, an *attitude determination and control subsystem* simulator build in Matlab/SimulinkTM will be presented. Initially it was tested in its dynamically decoupled version on the OUFTI-Next 3U CubeSat mission *phase A*, by the Centre Spatial de Liège (CSL) and the University of Liège, and then exploited to evidence the fine coupling between orbital and attitude dynamics in the ZodiArt iSEE mission. The simulator is characterised by a complete disturbances model, including: the Earth zonal harmonics, the Moon and Sun third body perturbations, solar radiation pressure, atmospheric drag and lift, capable of providing reliable and accurate results in terms of actuators and sensors sizing, as well as of mission operation simulations.

In Section 2 the theoretical description of the attitude-orbit coupled simulator architecture will be presented and in Section 3, the results regarding the fine coupling between orbital and attitude dynamics in the ZodiArt mission will be discussed.

2 The Attitude-Orbit Coupled Simulator Architecture

In this paper, three main reference systems will be used: the *inertial reference frame*, the non-inertial *body-fixed reference frame* and the *local vertical, local horizontal reference frame*. The first one has its origin in the centre of the Earth, its X-axis is oriented towards the vernal direction and the Z-axis is pointed towards the North Pole. The second reference frame instead is a non-inertial frame, centred in the spacecraft centre of mass and dependent on the platform considered. The last reference frame is also a non-inertial reference frame whose orthogonal unit vectors are $\hat{\mathbf{r}}$, $\hat{\mathbf{s}}$ and $\hat{\mathbf{w}}$, where $\hat{\mathbf{r}}$ is the osculating position vector direction. $\hat{\mathbf{w}}$, instead, is the unit vector normal to the osculating orbital plane, in the direction of angular momentum vector \mathbf{h} , the transverse vector $\hat{\mathbf{s}}$ is normal to both \mathbf{r} and $\hat{\mathbf{w}}$ and it therefore points in the direction of the orbiting body's local horizon, as shown in Figure 1.

The subscript $(\cdot)_{b/n}$, means a rotation from the *inertial reference frame*, indicated by n , to the *body-fixed reference frame*, indicated by b . $\mathbf{A}_{\mathbf{LVLH}}$, is referred to a rotation with respect to the *inertial frame* and can be also indicated as $(\cdot)_{l/n}$. As a result the following matrix multiplication can generate a rotation from the *local vertical, local horizontal reference frame* to *body-fixed reference frame*, $\mathbf{A}_{b/l}$:

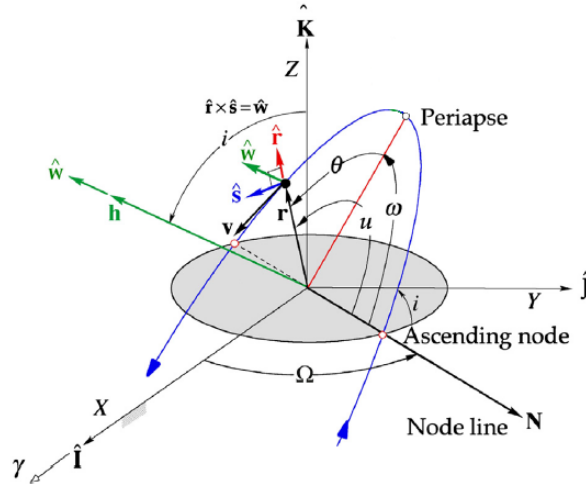


Fig. 1 The local vertical, local horizontal $\hat{f}\hat{s}\hat{w}$ frame, [4].

$$\mathbf{A}_{b/l} = \mathbf{A}_{b/n} \mathbf{A}_{l/n}^T \quad (1)$$

where $(\cdot)^T$ is the transpose of the matrix. Eq. 2 represents the transformation of a vector from the *Inertial reference frame* to the *body-fixed reference frame* and can be generalized to any kind of change of bases.

$$\mathbf{a}_b = \mathbf{A}_{b/n} \mathbf{a}_n \quad (2)$$

The attitude matrices were implemented exploiting the quaternion formulation, [11]:

$$\mathbf{A}_{b/n}(\mathbf{q}) = \begin{bmatrix} q_1^2 - q_2^2 - q_3^2 + q_4^2 & 2(q_1 q_2 + q_3 q_4) & 2(q_1 q_3 - q_2 q_4) \\ 2(q_1 q_2 - q_3 q_4) & -q_1^2 + q_2^2 - q_3^2 + q_4^2 & 2(q_2 q_3 + q_1 q_4) \\ 2(q_1 q_3 + q_2 q_4) & 2(q_2 q_3 - q_1 q_4) & -q_1^2 - q_2^2 + q_3^2 + q_4^2 \end{bmatrix} \quad (3)$$

where the quaternion components shall satisfy the constrain expressed in Eq.4:

$$q_1^2 + q_2^2 + q_3^2 + q_4^2 = 1 \quad (4)$$

2.1 Orbit-attitude disturbances

The disturbances model providing the perturbative accelerations and torques which respectively act on orbit and attitude dynamics are presented in Tab.1 and Tab.2, reporting also the models used and their references.

Table 1 Perturbative accelerations

Source	Model	Formulation	References
Earth zonal harmonics	7 th order Legendre Polynomials	$\mathbf{P}_{obl} = -\nabla\Phi$ $\Phi(r, \psi) = \frac{\mu}{r} \sum_{k=2}^{\infty} J_k \left(\frac{R}{r}\right)^k P_k(\cos\psi)^*$	[4]
Sun and Moon third body effect	Restricted Circular 3 Body Problem	$\mathbf{PRC3BP} = \mu_2 \left(\frac{\mathbf{r}_{21}}{r_{21}^3} - \frac{\mathbf{r}_2}{r_2^3} \right)^{**}$	[4]
Atmospheric drag and lift	Cannonball model	$\mathbf{P}_{drag} = -\frac{1}{2}\rho(h)C_d\frac{A_d}{m}\mathbf{v}_{rel}\ \mathbf{v}_{rel}\ ^{***}$ $\mathbf{P}_{lift} = \frac{1}{2}\rho(h)C_l\frac{A_d}{m}\frac{\mathbf{v}_{rel} \times (\mathbf{v}_{rel} \times \mathbf{n})}{\ \mathbf{v}_{rel} \times (\mathbf{v}_{rel} \times \mathbf{n})\ }\ \mathbf{v}_{rel}\ ^2$	[4] [10]
Solar radiation pressure	Flat plate model	$\mathbf{PSRP} = -\frac{P_{SR}}{m}C_rA_s\hat{\mathbf{S}}^{****}$	[4]

* with $\psi = \tan^{-1} \frac{\sqrt{x^2+y^2}}{z}$, where x , y and z are written in the Earth centred fixed reference frame and μ is the Earth planetary constant. J_k are the *zonal harmonics* of the planet, R is its equatorial radius ($R/r < 1$), and P_k are the Legendre polynomials: $P_k(x) = \frac{1}{2^k k!} \frac{d^k}{dx^k} (x^2 - 1)^k$.

** \mathbf{r}_2 and r_2 are respectively the second body (Moon or Sun) position vector and the distance from the center of the main attractor, the Earth, while \mathbf{r}_{21} and r_{21} are respectively the second body position vector and the distance from the spacecraft. The second body planetary constant is indicated with μ_2 .

*** where: $\rho(h)$ is atmospheric density model, dependent on altitude h ; C_d is the drag coefficient (Both for OUFTI-Next CubeSat and ZodiArt platform, it was considered equal to 2.2, respectively from [6] and from extrapolation of data by [8]); A_d is the platform surface exposed to the relative wind; $\mathbf{v}_{rel} = \mathbf{v} - \mathbf{v}_{atm}$ is the wind relative velocity, obtained as vectorial difference between the spacecraft velocity and the atmospheric velocity vector, \mathbf{v}_{atm} , both in the *Inertial reference system*. The lift coefficient was obtained from $C_l = 2\sin(\alpha)\sin(\alpha)$, under the *specular reflection* assumption above 800 km, [14], where α is the bus angle of attack. The model used for atmospheric density is an exponential model reported in [5]: $\rho = \rho_0 \exp\left[-\frac{h-h_0}{H}\right]$, where ρ_0 is reference density, h_0 the reference altitude and H is the scale height.

**** P_{SR} is the solar radiation pressure, whose value is 4.56×10^{-6} N/m² (4.56 μ Pa); m is the mass of the spacecraft; C_r is the reflective coefficient, whose value spans between 1 (black body) and 2 (ideal reflector) for a flat surface, while it is always 1 for a sphere, [7]; $\hat{\mathbf{S}}$ is the satellite-Sun unit vector in the *inertial reference frame*. To simulate more precisely this effect, a cylindrical eclipse model was implemented, as presented in [5].

Table 2 Perturbative torques

Source	Model	Formulation	References
Geomagnetic field	Magnetic field model by Matlab TM build-in function <i>wrldmagn.m</i>	$\mathbf{B}_b = \mathbf{A}_{b/n} \mathbf{B}_n$ $\mathbf{T}_{\text{magnetic}} = \mathbf{m} \times \mathbf{B}_b^*$	[6]
Gravity gradient	Integral torque	$\mathbf{T}_{\text{gravity}} = \frac{3\mu}{r^5} \int_M (\mathbf{r}_b \cdot \mathbf{r})(\mathbf{r}_b \times \mathbf{r}) dm =$ $= -\frac{3\mu}{R^3} \begin{bmatrix} (I_3 - I_2) \hat{r}_y \hat{r}_z \\ (I_1 - I_3) \hat{r}_x \hat{r}_z \\ (I_2 - I_1) \hat{r}_x \hat{r}_y \end{bmatrix}^{**}$	[4]
Atmospheric drag	Flat plate model	$\mathbf{T}_{\text{drag}} = \begin{cases} -\frac{1}{2} \rho(h) C_d v_{rel}^2 \frac{\mathbf{v}_{rel}}{\ \mathbf{v}_{rel}\ } \sum_{i=1}^N \mathbf{r}_{cp,i} \times (\mathbf{n}_i \frac{\mathbf{v}_{rel}}{\ \mathbf{v}_{rel}\ }) A_i^{***} \\ (\mathbf{n}_i \frac{\mathbf{v}_{rel}}{\ \mathbf{v}_{rel}\ }) > 0 \end{cases}$	[9]
Solar radiation pressure	Flat plate model	$\mathbf{F}_{\text{SRP}} = P_{SR} A_s [\rho_a (\hat{\mathbf{S}} \cdot \mathbf{n}) + 2\rho_s (\hat{\mathbf{S}} \cdot \mathbf{n})^2 \cdot \mathbf{n} + \frac{2}{3} \rho_d (\hat{\mathbf{S}} \cdot \mathbf{n})]$ $\mathbf{T}_{\text{SRP}} = \begin{cases} \sum_{i=1}^N \mathbf{r}_{cp,i} \times \mathbf{F}_{\text{SRP}_i} & **** \\ (\hat{\mathbf{S}} \cdot \mathbf{n}) > 0 \end{cases}$	[9]

* \mathbf{B}_b and \mathbf{B}_n are respectively the magnetic field vector in body and inertial reference frame, while \mathbf{m} is the platform internal magnetic induction.

** where M is the spacecraft total mass, \mathbf{r} is the satellite osculating position vector and \mathbf{r}_b is the vector connecting its centre of mass to the infinitesimal cube of mass dm . It is possible to express the torque in function of the position unit vector $\hat{\mathbf{r}}$ and the spacecraft inertias along the principal axes, $I_{1,2,3}$.

*** To obtain the overall torque vector acting on the spacecraft, \mathbf{p}_{drag} is multiplied by the spacecraft mass; then, the cross-product between the resulting force and the vector connecting the centre of mass and the assumed centre of pressure, \mathbf{r}_{cp} , is performed. Since its position is uncertain or dependent on time, a 10% error was considered. Obviously, if the product between the surface's normal and the relative velocity is less than 0, the resulting torque is null. N is the number of spacecraft surfaces and \mathbf{n}_i the normal to the surface i .

**** where: \mathbf{n} is the surface normal vector; ρ_a , ρ_d and ρ_s are the surface absorption, diffusive and scattering coefficients respectively. As for the drag, in order to obtain the overall torque, a multiplication times the arm is required and, as before, a 10% error was considered in the position of the centers of pressure on the N platform surfaces.

2.2 Sensors and attitude determination algorithm

The sensors model and attitude determination algorithm implemented in the simulator introduce noises and measurement errors in the integrated states, to simulate the sensors' accuracy effect and then to reconstruct the state, thanks to the determination algorithm. Firstly the sensors were modeled and then an *Unscented Kalman filter* was implemented, selected because, differently from the *Extended Kalman filter*, it does not rely on the system linearisation, but on *unscented transformations*.

2.3 Control

The control law selected for the simulator is a Proportional and Derivative law (PD) driving the dynamics of 3 reaction wheels oriented as the spacecraft principal axes (configuration matrix equal to the identity matrix: $\mathbf{A} = \mathbf{I}_{3 \times 3}$). The Integrative term of a classic PID controller was discarded in order to speed up the code, since no beneficial effect from the controllability point of view was evidenced once implemented. According to the stability theory of non linear systems [11], the control law of a PD controller shall be based on a Lyapunov function, $\Gamma(\mathbf{x})$, dependent on the state \mathbf{x} and based on the kinetic energy related to the Euler system of equations, Eqs.16 to 18, which represent the spacecraft attitude dynamics.

$$\Gamma(\boldsymbol{\omega}, \mathbf{q}) = \frac{1}{2}(I_1 \omega_{b1}^2 + I_2 \omega_{b2}^2 + I_3 \omega_{b3}^2) + \gamma(\mathbf{q}) \quad (5)$$

In order to assure Lyapunov stability the following relations have to be satisfied:

- $\Gamma(\mathbf{x}) > 0, \forall \mathbf{x} \neq \mathbf{x}_{eq}$
- $\Gamma(\mathbf{x}) = 0, \text{ for } \mathbf{x} = \mathbf{x}_{eq}$
- $\dot{\Gamma}(\mathbf{x}) \leq 0$

where \mathbf{x}_{eq} is an equilibrium point, in this particular case characterised by $\boldsymbol{\omega}_b = \boldsymbol{\omega}_{b,d}$ and $\mathbf{q}_e = [0 \ 0 \ 0 \ 1]^T$. In particular:

- $\boldsymbol{\omega}_b$ and $\boldsymbol{\omega}_{b,d}$ respectively, the actual and target spacecraft angular velocities.
- \mathbf{q}_e is the error quaternion between the actual attitude matrix, $\mathbf{A}_{b/n}$, and the desired one, \mathbf{A}_d , transformed in quaternions.

In order to find the error quaternion to be driven to zero, \mathbf{q}_e , the following steps are requested:

1. Transform the \mathbf{A}_d matrix in control quaternion: \mathbf{q}_c .
2. Compute the error between the actual quaternion \mathbf{q} and the control one \mathbf{q}_c , exploiting the quaternion multiplication:

$$\mathbf{q}_e = (\mathbf{q}_c)^{-1} \otimes \mathbf{q} = \begin{bmatrix} q_{4c} & q_{3c} & -q_{2c} & -q_{1c} \\ -q_{3c} & q_{4c} & q_{1c} & -q_{2c} \\ q_{2c} & -q_{1c} & q_{4c} & -q_{3c} \\ q_{1c} & q_{2c} & q_{3c} & q_{4c} \end{bmatrix} \mathbf{q} \quad (6)$$

Where, if $\mathbf{q}_c = [0 \ 0 \ 0 \ 1]^T$, it means that $\mathbf{q}_e = \mathbf{q}$.

For the simulator implemented, the method to represent the reference frame are the quaternions and, as a consequence, it was selected a Lyapunov function based on the scalar number of the error quaternion, $q_{e,4}$:

$$\gamma(q_{e,4}) = 1 - q_{e,4}^2 \quad (7)$$

This particular law was selected since it is immune to *unwinding*, which is a typical issue, when quaternions are exploited [11]. The square in the law has the role to make the Lyapunov function independent from the sign of $q_{e,4}$

Once the control law is selected, the control torque \mathbf{u} will be:

$$\mathbf{u} = K_p \frac{\partial \gamma}{\partial q_{e,4}} \mathbf{q}(1,2,3) + K_d (\boldsymbol{\omega}_{\mathbf{b},\mathbf{d}} - \boldsymbol{\omega}_{\mathbf{b}}) \quad (8)$$

$$\mathbf{u} = -2K_p \mathbf{q}_{e,4} \mathbf{q}_e(1,2,3) + K_d (\boldsymbol{\omega}_{\mathbf{b},\mathbf{d}} - \boldsymbol{\omega}_{\mathbf{b}}) \quad (9)$$

where K_p and K_d are respectively the proportional and derivative constants, both positive. They will be obtained through single and double objective optimisations, depending on the mission and on the single phase.

2.4 The mathematical model

The whole set of attitude-orbit coupled differential equations are here reported, where I_i are the spacecraft inertias along the principal axis (indicated with subscripts 1, 2, 3), r , the osculating position vector magnitude, \mathbf{u} the control torque, \mathbf{d} the disturbances torque, \mathbf{A} the reaction wheels configuration matrix. In particular, the orbital dynamics was coupled through the perturbative acceleration induced by atmospheric drag, lift and solar radiation pressure. Gauss planetary equations [4], Eqs.10 to 15, drive the orbital dynamics, providing 6 states: the orbital momentum h_m , the eccentricity e , the right ascension of the ascending node Ω , the anomaly of the perigee ω and the true anomaly θ . Then, the attitude dynamics is driven by the Euler equations, Eqs.16 to 18, the quaternion integration, Eq.19, and the reaction wheels momenta equation, Eq.20, as reported in [11] and providing 10 states: the three components of the angular velocity vector $\boldsymbol{\omega}_{\mathbf{b}}$, the four components of the quaternion \mathbf{q} and the reaction wheels momenta three components \mathbf{h}_r .

$$\dot{h}_m = r p_s \quad (10)$$

$$\dot{e} = \frac{h_m}{\mu} \sin \theta p_r + \frac{1}{\mu h_m} [(h_m^2 + \mu r) \cos \theta + \mu e r] p_s \quad (11)$$

$$\dot{\theta} = \frac{h_m}{r^2} + \frac{1}{e h_m} \left[\frac{h_m^2}{\mu} \cos \theta p_r - \left(r + \frac{h_m^2}{\mu} \right) \sin \theta p_s \right] \quad (12)$$

$$\dot{\Omega} = \frac{r}{h_m \sin i} \sin(\omega + \theta) p_w \quad (13)$$

$$\dot{i} = \frac{r}{h_m} \cos(\omega + \theta) p_w \quad (14)$$

$$\dot{\omega} = -\frac{1}{e h} \left[\frac{h_m^2}{\mu} \cos \theta p_r - \left(r + \frac{h_m^2}{\mu} \right) \sin \theta p_s \right] - \frac{r \sin(\omega + \theta)}{h_m \tan i} p_w \quad (15)$$

$$\dot{\omega}_{b1} = \frac{I_2 - I_3}{I_1} \omega_{b2} \omega_{b3} + \frac{u_1 + d_1}{I_1} \quad (16)$$

$$\dot{\omega}_{b2} = \frac{I_3 - I_1}{I_2} \omega_{b1} \omega_{b3} + \frac{u_2 + d_2}{I_2} \quad (17)$$

$$\dot{\omega}_{b3} = \frac{I_1 - I_2}{I_3} \omega_{b2} \omega_{b1} + \frac{u_3 + d_3}{I_3} \quad (18)$$

$$\dot{\mathbf{q}} = \frac{1}{2} \begin{bmatrix} 0 & \omega_{b3} & -\omega_{b2} & \omega_{b1} \\ -\omega_{b3} & 0 & \omega_{b1} & \omega_{b2} \\ \omega_{b2} & -\omega_{b1} & 0 & \omega_{b3} \\ -\omega_{b1} & -\omega_{b2} & -\omega_{b3} & 0 \end{bmatrix} \mathbf{q} \quad (19)$$

$$\dot{\mathbf{h}}_{\mathbf{r}} = \mathbf{A}^{-1}(\mathbf{A}\mathbf{h}_{\mathbf{r}} \times \boldsymbol{\omega}_{\mathbf{b}} - \mathbf{u}) \quad (20)$$

The perturbative vector \mathbf{p} is the sum of the perturbative accelerations presented in Section 2.1 and decomposed in the *local vertical, local horizontal reference frame*. The accelerations due to the lift, drag and solar radiation pressure depend on the cross surfaces exposed to the atmospheric and solar wind, as shown in Section 2.1, function of the spacecraft's attitude through the exposed surfaces normal unit vectors \mathbf{n}_i and this new dependency couples the orbital dynamics with the attitude one. This is clearly visible in, Eqs.21 to 23, where, in particular in the first two equations,

$$0 \leq \mathbf{n}_i \cdot \frac{\mathbf{v}_{\text{rel}}}{\|\mathbf{v}_{\text{rel}}\|} \leq 1$$

identifies the portion of cross surfaces exposed to the atmospheric wind, when multiplying the exposed surfaces $A_{d,i}$, while in the last one, the scaling factor for $A_{s,i}$ is $(\hat{\mathbf{S}} \cdot \mathbf{n}_i)$. The number of surfaces characterising the spacecraft is indicated as N .

$$\mathbf{p}_{\text{drag}} = -\frac{1}{2}\rho(h)\frac{C_d}{m}\sum_i^N A_{d,i}\left(\mathbf{n}_i \cdot \frac{\mathbf{v}_{\text{rel}}}{\|\mathbf{v}_{\text{rel}}\|}\right)\mathbf{v}_{\text{rel}}\|\mathbf{v}_{\text{rel}}\| \quad (21)$$

$$\mathbf{p}_{\text{lift}} = \frac{1}{2}\rho(h)\frac{C_l}{m}\sum_i^N A_{d,i}\left(\mathbf{n}_i \cdot \frac{\mathbf{v}_{\text{rel}}}{\|\mathbf{v}_{\text{rel}}\|}\right)\frac{\mathbf{v}_{\text{rel}} \times (\mathbf{v}_{\text{rel}} \times \mathbf{n}_i)}{\|\mathbf{v}_{\text{rel}} \times (\mathbf{v}_{\text{rel}} \times \mathbf{n}_i)\|}\|\mathbf{v}_{\text{rel}}\|^2 \quad (22)$$

$$\mathbf{p}_{\text{srp}} = \frac{P_{SR}}{m}\sum_i^N A_{s,i}\left[\rho_a(\hat{\mathbf{S}} \cdot \mathbf{n}_i) + 2\rho_s(\hat{\mathbf{S}} \cdot \mathbf{n}_i)^2 \cdot \mathbf{n} + \frac{2}{3}\rho_d(\hat{\mathbf{S}} \cdot \mathbf{n}_i)\right] \quad (23)$$

In conclusion, there are 16 first order differential equations and, as a consequence, 16 states to be integrated.

3 Application to the ZodiArt iSEE Mission

The Global Sustainable Development Goals [12] are 17 objectives addressing the global challenges such as poverty, inequality, climate, environmental degradation,

prosperity, peace and justice and they are the focus of the ZodiArt iSEE project. This mission is characterised by a set of MicroSat flying in formation and constituting an artificial constellation in the sky, easily recognisable from ground. This is possible thanks to high reflective balloons embarked on the top of platforms. People can interact with the system using a mobile app to prove the fulfilment of the Global Sustainable Development Goals, obtaining from the constellation a picture of the surroundings, when the formation will pass above the user. The orbit was identified after a trade-off analysis presented in [1] and [2], providing good visibility from the most important cities of the world during the twilight. The constellation will generally point the Nadir direction, performing Earth observation. In this section, the dynamics of the platform will be discussed in different perturbed scenarios, characterised by the Earth zonal harmonics, the Moon and Sun third body perturbations, solar radiation pressure, drag and lift effects, with the aim to build an *orbital long-track envelope*, useful to plan attitude manoeuvres, capable of performing fine relative positioning in the context of formation flying.

With respect to a reference configuration, the platform exposing the maximum surface to the atmospheric and solar wind lowers the orbit semi-major axis, due to the resulting increase of the drag and solar radiation pressure, while the one exposing the minimum area lowers it. According to elementary orbital dynamics, if two bodies are orbiting with different altitudes around the same attractor, they will experience a long-track drift, proportional to the difference in altitude. In particular the body characterised by an higher orbit will shift in the backward direction with respect to the other body and viceversa.

Performing differential drag/lift, means that the satellite will be exposed to the relative atmospheric wind, in order to achieve a desired long-track position and a certain altitude with respect to an other orbiting body, which, in this case, is another satellite of the constellation. Nevertheless, the same concept can be applied to solar radiation pressure.

3.1 Differential drag/lift

Usually in literature the most exploited natural perturbation to control a spacecraft is the atmospheric drag only, as reported for instance in [13]. In this paper both lift and drag were considered and their effects evaluated performing many simulations, varying: the initial epoch, spanning from the 6th of December 2018 to the 21st of November 2019, with a time interval of 15 days, and the cross exposed area, spanning from 0° to 90° the bus inclination with respect to the velocity vector, since the balloon exposed surface is always the same. This was performed with respect to a reference configuration attitude, inclined of 45°, over one orbital period. The results are collected in Figure 2, that represents the *Orbital long-track envelope*, showing the differential height and shift achieved performing a differential drag/lift manoeuvre, under the effect of all the previously mentioned perturbances, at different epochs, in function of the platform angle of attack and given the initial true anomaly.

Figure 2 also evidences, as expected, that differential drag/lift is independent on the

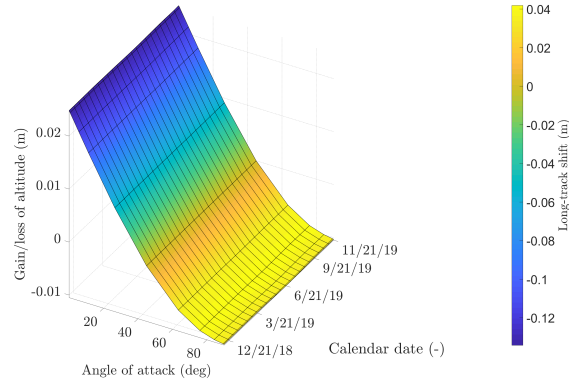


Fig. 2 *Orbital long-track envelope related to drag/lift effects only.*

initial epoch. Moreover, the gain in altitude, and the consequent backward shift, are higher with respect to the altitude loss and advancing shift. This is due to the fact that, in the first case, the dynamics is evolving in the same direction of drag, while in the second case it is counteracted by the atmospheric wind.

The increase/decrease in altitude after one period is quite small compared to the one achievable at lower orbits, with solar sails, but it can be still exploited, especially if the differential drag manoeuvre lasts longer.

3.2 *Solar radiation pressure*

Solar radiation pressure effect is strictly related to the Sun position with respect to the orbital plane, resulting in a high dependence on the initial epoch. The very same set of simulations were performed also in the case of only solar radiation pressure effect, resulting in a more complex dynamics, due to the fact that the exposed surface orientation is not optimised to point the Sun, but it is oriented almost towards the relative atmospheric wind. The results achieved are shown in Figure 3. It is possible to notice that, close to the spring and autumn equinoxes, the effects of solar radiation pressure are the lowest, since the Sun is almost orthogonal to the orbital plane, acting mostly on the cross-track orbital evolution, rather than the long-track one.

However, the most interesting effect that the plot evidences, is that the gain/loss in altitude, and correspondent shift, experienced close to the summer solstice are not the same evidenced during the winter solstice. Close to these two dates, the orbit is half in light and half in eclipse, with the Sun illuminating one of the two orbital semi-circumferences depending on the date considered and, according to

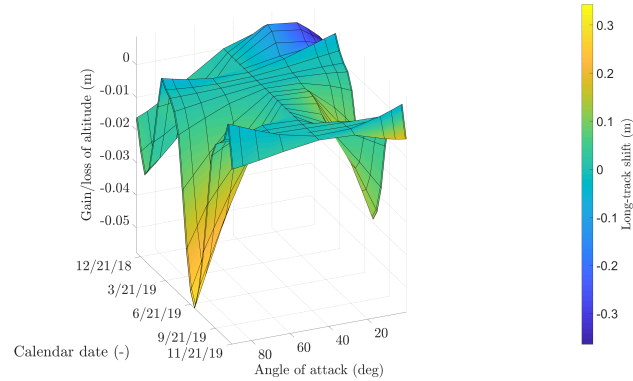


Fig. 3 *Orbital long-track envelope* related to solar radiation pressure effect only. The spacecraft, at the beginning of the manoeuvre, is characterised by declination almost null in eclipse.

this scenario, the spacecraft dynamics should be the same. Nevertheless, what is changing is the illumination condition of the satellite when the manoeuvre starts: in the case reported in Figure 3, during the summer solstice, ZodiArt platform begins its manoeuvre in eclipse, with declination almost null, meaning that, after less than a quarter of orbit, it will start to experience solar radiation pressure, accelerating while covering the illuminated part of orbit, and finally continuing to slightly move in the direction of perturbation once entered in eclipse, due to the inertia acquired. During the winter solstice, on the contrary, the spacecraft is characterised by almost null declination but it is in Sun-light, meaning that the perturbative acceleration will affect the spacecraft for slightly more than a quarter of orbit, then it will enter in eclipse and finally it will experience again the solar wind pressure. This means that, in the second case, the platform can not continuously accelerate in the illuminated half of orbit, resulting in a reduced gain/loss of altitude. The proof of what just discussed can be find varying the initial true anomaly, as shown in Figure 4: the results are reported in Figure 5.

In particular:

- At $\theta_0 = 90^\circ$, the 21st of June 2019, the platform starts the manoeuvre just at the end of the eclipse, maximising the acceleration due to solar radiation pressure and, as a result, the deepest peak is reached.
- At $\theta_0 = 180^\circ$, the dynamics is exactly the opposite of the one shown in Figure 3, since the spacecraft has declination almost null, but starts the manoeuvre 180° after on orbit.
- At $\theta_0 = 270^\circ$, the dynamics is the opposite to the $\theta_0 = 90^\circ$ case, since the spacecraft can exploit the overall perturbative acceleration only during the winter solstice.

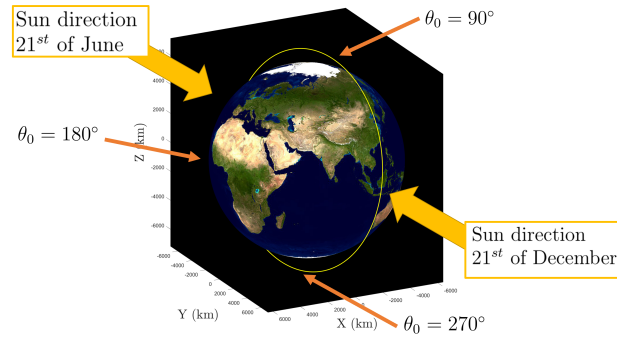


Fig. 4 Orbit and platform Sun exposition depending on θ_0 and date.

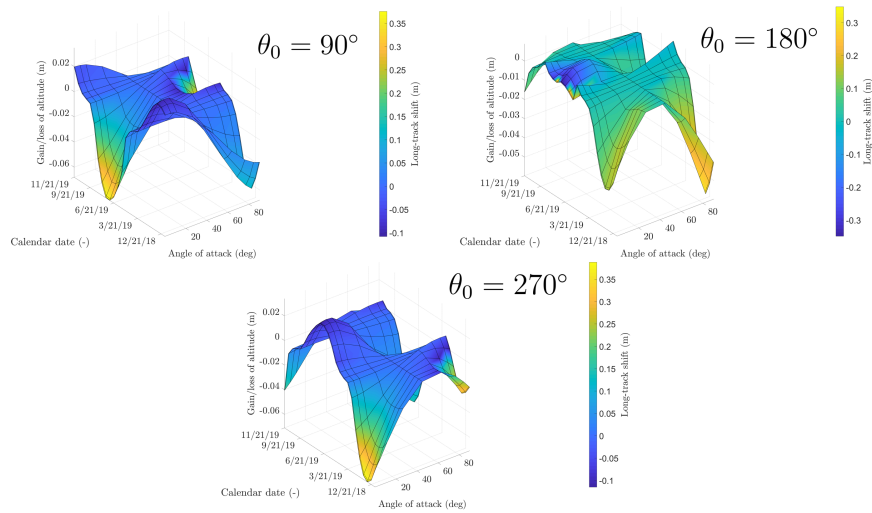


Fig. 5 Orbital long-track envelope related to solar radiation pressure effect only at different initial true anomalies, θ_0 .

3.3 Solar radiation pressure and drag/lift effects

It was shown that solar radiation pressure is the perturbative acceleration that mostly affect the differential dynamics, but in the case of equinoxes, when the Sun direction is almost orthogonal to the orbital plane, differential drag/lift are the main actors rising and lowering the altitude. In Figure 6, the cumulative effects of solar radiation pressure and drag/lift are reported referred to null initial true anomaly. It is possible to appreciate that, in correspondence of equinoxes, the gain and loss in altitude are the same achievable with differential drag only, while in the remaining periods of the year, the solar radiation pressure is the driving perturbation. In the case of different

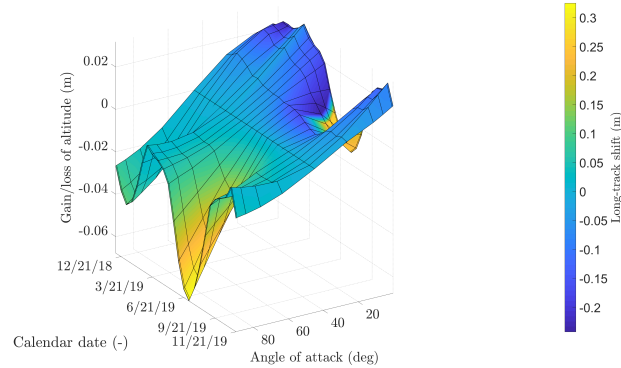


Fig. 6 Orbital long-track envelope related to solar radiation pressure and lift/drag effects. Initial true anomaly, θ_0

initial true anomalies, the same trend evidenced with the *solar radiation pressure long-track envelopes* is obtained.

3.4 Long-term differential drag

It was demonstrated that, during equinoxes, differential drag can be exploited, independently from solar radiation pressure, to control the spacecraft. However, the differential height and shift acquired are quite small compared to the ones achievable at lower orbits and equipped with solar sails. For this reason, long-term differential drag/lift manoeuvres can be inspected to increase the effects of these perturbation. To test one of these manoeuvres, a reference scenario was selected: three simulations, with the same initial condition but the initial orientation with respect to the velocity vector (\mathbf{q}_0), were performed over 10 orbital periods with initial epoch at the spring equinox. In particular:

- The *reference configuration*: tilted of 45° with respect to the velocity vector.
- The *advancing configuration*: characterised by the maximum exposed surface, which will lower the altitude and shift in the same direction of velocity vector.
- The *receding configuration*: characterised by the minimum surface exposed, which will rise the altitude and shift in the opposite direction of velocity vector.

Together with solar radiation pressure and drag/lift, also the Earth oblateness and the Moon/Sun third body perturbation were considered. The simulations reported a gain in altitude of 0.29 m with a backward shift of -12.6 m and a loss in altitude of -0.12 m with a frontward shift of 3.9 m.

4 Conclusions

Thanks to the work done on the ZodiArt iSEE project it was possible to test the attitude-orbit coupled simulator, characterised by the presence of all the major disturbances experienced on orbit and capable to handle also the low and fine coupling between attitude and orbital dynamics. The tool developed can provide *Orbital long-track envelopes*, representing the differential height and shift achieved performing a differential drag/lift manoeuvre under the effect of all the previously mentioned perturbances, at different epochs, in function of the platform angle of attack and given the initial true anomaly. Finally, a simulation of a long-term manoeuvre, lasting 10 orbital periods, was presented. The analyses performed can be easily generalised to any kind of spacecraft and orbit.

References

1. Colombo C. Dal Monte L.: ZodiArt iSEE mission. Technical Report (2017)
2. Roccioletti, M.P.: Mission Analysis and concept design for a reflective balloon mission. Master Thesis, Politecnico di Milano (2018), Supervisor: Camilla Colombo
3. Palais R. Rodi S. Palais B.: A Disorienting Look at Euler's Theorem on the Axis of a Rotation, *The American Mathematical Monthly* 116.10 (2009), pp. 892909
4. Curtis, H., *Orbital Mechanics: for Engineering Students*, Second Edition, Butterworth Heine-mann, Aerospace Engineering (2010)
5. D.D. Vallado: *Fundamentals of Astrodynamics and Applications*, Space Technology Series, McGraw Hill (1997)
6. Wertz, J. R., *Space Mission Analysis and Design*, Ed. 3, Space Technology Library (1999)
7. Bewick, C., *Space mission applications of high area-to-mass-ratio orbital dynamics*, University of Strathclyde, Engineering (2013)
8. Bowman, B.R., Kenneth M.: Drag coefficient variability at 175-500km from the orbit decay analyses of spheres, AAS 2005-257, AAS/AIAA Astrodynamics (2005)
9. Bong, W.: *Space Vehicle Dynamics and Control*, AIAA Education Series, (2006)
10. Nikolaev S. Pertica A. Horsley M.: *Rendezvous Maneuvers of Small Spacecraft Using Differential Lift and Drag*. Tech. rep., Lawrence Livermore National Laboratory (LLNL), Livermore, CA, (2011)
11. Schetz, J. A.: *Analytical Mechanics of Space Systems*, Third Edition, AIAA Education Series (2014)
12. About the Sustainable Development Goals. (2018) <https://www.un.org/sustainable-development/>
13. Pini, G.: Long-Term Cluster Flight of Multiple Satellites Using Differential Drag, *Journal of Guidance Control and Dynamics*, Vol. 36, No.6, pp.1731-1740, doi:10.2514/1.61496. (2013)
14. Pulido, C. L.: *Aerodynamic Lift and Drag Effects on the Orbital Lifetime Low Earth Orbit (LEO) Satellites*, University of Colorado Boulder (2007)
15. Moore, P.: The effect of aerodynamic lift on near-circular satellite orbits, *Planetary and space science*, 33(5), 479-491 (1985)

Glossary

- A** Constant reaction wheels configuration matrix.
- $\mathbf{A}_{b/l}$ Rotation matrix from local to body-fixed frame.
- $\mathbf{A}_{b/n}$ Rotation matrix from inertial to body-fixed frame.
- A_d Area exposed to the atmospheric wind.
- A_s Area exposed to the Sun radiation.
- \mathbf{B}_b Magnetic field vector in body fixed frame from magnetometers.
- \mathbf{B}_n Magnetic field vector in inertial frame.
- C_d Hypersonic drag coefficient.
- C_l Hypersonic lift coefficient coefficient.
- C_r Reflective coefficient.
- \mathbf{F}_{drag} Drag force.
- J_k Zonal harmonics term.
- K_p Proportional constant for PD controller.
- K_d Derivative constant for PD controller.
- P_k Legendre polynomial term.
- P_{SR} Solar radiation pressure.
- $\hat{\mathbf{S}}$ Satellite-Sun unit direction in *inertial reference frame*.
- \mathbf{T}_{drag} Torque due to drag.
- \mathbf{T}_{SRP} Solar radiation pressure resulting torque.
- $\mathbf{T}_{\text{magnetic}}$ Torque due to Earth magnetic field interaction.
- $\mathbf{T}_{\text{gravity}}$ Torque due to gravity gradient.

V Earth magnetic field potential.

a Semi-major axis.

\mathbf{d} Disturbances torque.

e Eccentricity.

h Height.

h_0 Reference height.

\mathbf{h}_m Angular momentum vector in inertial reference frame.

\mathbf{h}_r Reaction wheels angular momentum.

i Inclination.

m Mass.

\mathbf{m} Residual dipole moment.

\mathbf{n} Normal vector.

\mathbf{p} Perturbative vector in inertial reference frame.

\mathbf{p}_{drag} Perturbative vector due to atmospheric drag in inertial reference frame.

\mathbf{p}_{obl} Perturbative vector due to Earth oblateness in inertial reference frame.

\mathbf{p}_{RC3BP} Perturbative vector due to third body perturbation in inertial reference frame.

\mathbf{p}_{SRP} Perturbative vector due to solar radiation pressure in inertial reference frame.

\mathbf{q} Quaternion.

\mathbf{q}_c Control quaternion.

\mathbf{q}_e Quaternion error.

\mathbf{r} Osculating position vector in inertial reference frame.

\mathbf{r}_b Vector connecting the spacecraft centre of mass to the infinitesimal cube of mass dm .

\mathbf{r}_{cp} Vector connecting the spacecraft centre of mass to the centre of pressure.

\mathbf{v} Velocity vector in inertial reference frame.

\mathbf{v}_{atm} Earth atmospheric velocity vector.

\mathbf{v}_{rel} Relative velocity vector.

t time.

\mathbf{u} Control torque.

Γ Lyapunov function.

α Angle of attack.

γ Lyapunov function term dependent on the quaternion.

θ True anomaly.

μ Planetary constant.

Φ Perturbation of the gravitational potential due to planet oblateness.

ρ Atmospheric density.

ρ_a Surface absorption coefficient.

ρ_d Surface diffusive coefficient.

ρ_s Surface scattering coefficient.

ψ Polar angle.

ω Anomaly of the perigee.

$\omega_{\mathbf{b}}$ Angular velocity vector.

$\omega_{\mathbf{b},\mathbf{d}}$ Desired angular velocity vector.